Rational surfaces, flows and radial structure in the TJ-II stellarator

B.Ph. van Milligen[1], I. Voldiner[1], B.A. Carreras[2,3], L. García[2], M.A. Ochando[1] and the TJ-II Team

[1] National Fusion Laboratory, CIEMAT, Madrid, Spain
[2] Departamento de Física, Universidad Carlos III de Madrid, Leganés, Madrid, Spain
[3] Department of Physics, University of Alaska, Fairbanks, Alaska

Abstract. In this work, we report on the results obtained by measuring several turbulent quantities well inside the plasma edge by means of a Langmuir probe during dynamical rotational transform scans in the TJ-II stellarator, while applying a radial electric field to the edge plasma using a biasing probe. By calculating the intermittence parameter from floating potential measurements, we are able to identify a major low order rational surface and hence relate the probe measurements to the local value of the rotational transform.

Based on the former, we are able to show that the poloidal plasma velocity (and hence radial electric field) has a significant radial structure that is clearly related to the rotational transform profile and in particular the lowest order rational surfaces in the range studied. The poloidal velocity is also affected by the edge biasing. The particle flux Γ was also found to exhibit a radial pattern, as did the flow shear suppression term $\omega_{E\times B}$, but the relation of the former to the low-order rational surfaces was less clear. We surmise that this lack of direct correspondence is due to an unknown term in the turbulence evolution equation: the instability growth rate, γ.

We make use of a reduced Magnetohydrodynamic turbulence model to interpret the results. Overall, a picture is obtained in which the plasma self-organizes towards a state with a clear radial pattern of the radial electric field, in line with expectations from some numerical studies describing the spontaneous formation of an '$E \times B$ staircase', consisting of alternating layers with fast and slow radial transport. In this state, the radial profiles of various quantities (density, temperature, pressure) will not be smooth.

1. Introduction

Fusion plasmas are complex, open systems subject to a strong external drive, pushing them to a state far from thermodynamic equilibrium. Such systems are characterized by the spontaneous appearance of structures [1], like the well-known zonal flows in the plasma edge that play a major role in the important Low to High (L to H) confinement transition [2].

The appearance of structures is however not limited to the plasma edge region. Stability analysis of pressure gradient driven Magneto-Hydrodynamic (MHD) turbulence has shown that the radial pressure profile will tend to develop 'flat spots' at the most unstable locations (singular or rational surfaces) [3, 4]. Theoretically, the resulting pressure profile is therefore expected to look like a 'staircase' rather than the often assumed smooth curve. Such non-smooth pressure profiles would imply a significant departure from the standard approach to radial (heat and particle) transport, as transport coefficient profiles would then likewise be non-smooth and dependent on the main local instabilities.

Very little experimental information is available on this issue, due to the difficulty of obtaining the required high resolution data inside the hot and turbulent plasma. Early work at the RTP tokamak, based on electron temperature measurements combined with a scan of the Electron Cyclotron Resonant Heating (ECRH) power deposition location, revealed the existence of a succession of temperature steps associated with low order rational surfaces [5]. Subsequently, an ad-hoc transport model was proposed to model the observed behaviour, characterized by sharp reductions of the heat transport coefficient at the rational surfaces [6].

In recent work, we investigated radial heat transport using an analysis technique based on the transfer entropy, applied to Electron Cyclotron Emission (ECE) measurements of the electron temperature T_e [7]. This allowed us to document the existence of minor transport barriers (which would result in 'staircase' profiles) in both the W7-X and TJ-II stellarators, with additional experimental evidence of 'jumping' transport behaviour corresponding to transport events crossing the semi-penetrable barriers [7]. Note that the cited experimental results all correspond to relatively low density plasmas, heated mainly using ECRH.

Similar observations were also made in flux-driven gyrokinetic turbulence models. In this context, the phenomenon was named the '$E \times B$ staircase' [8, 9]. The cited work shows the spontaneous formation of profile steps, associated with radial electric field corrugations or zonal flows. These steps were not always linked to rational surfaces. This linking may depend on the type of turbulence involved (ITG, ETG, TEM, etc.) and the plasma conditions (collisionality, etc.); something that is still largely unclear.

The existence of the 'staircase' would have a significant impact on our understanding of transport in the interior of the plasma: it would consist of alternating radial layers with rapid radial transport (possibly dominated by 'streamers', 'bursty transport' or 'ballistic events') and 'minor transport barriers' (zones with zonal flow

shear and significantly reduced turbulent transport, characterized by 'particle trapping effects'). The standard description of transport in terms of smooth profiles and smooth radial electric fields and transport coefficients would be inadequate to model this situation. Interestingly, the 'minor transport barriers' could possibly be manipulated through the reinforcement of the associated zonal flows.

If the 'staircase' phenomenon is assumed to be common, as has been suggested, this raises the question why reports in literature are so very scarce. We believe this is due mainly to the lack of experimental observations in the plasma core region with sufficient radial resolution and accuracy to resolve the relatively small profile steps. Observation is also made more difficult due to the omnipresence of turbulence. In addition, it may be that in higher density plasmas, the phenomenon becomes less intense, although this is not entirely clear.

Changes in the pressure gradient should generally be associated with corresponding changes in the radial electric field, E_r. It is probably easier to detect the 'staircase' using measurements of E_r (or, equivalently, the plasma potential or the poloidal or perpendicular velocity) than by direct measurement of the pressure, density, or temperature profiles, as argued in Section 4. This is the approach we followed in the present work.

The experimental results reported here provide extremely detailed information regarding the structure of the poloidal velocity (equivalent to E_r) at the TJ-II stellarator [10]. This structure is clarified by scanning the rotational transform profile dynamically during a discharge, while a Langmuir probe performed measurements at a fixed location well inside the plasma. Measuring at a fixed location offers the advantage that many quantities relevant to turbulence (such as the gradients) are nearly constant. This scan allowed exploring the behaviour of several important quantities across a range of rotational transform values. In addition, a biasing probe was used to manipulate the poloidal rotation velocity of the plasma. We calculated a quantifier of intermittence from the plasma potential fluctuations measured by the probe [11]. This quantifier responds to both plasma velocity and the presence of dominant low order modes, and allowed us to determine the time of passage of an important low order rational surface across the probe location. Thus, we could relate the plasma rotation profile to the structure of rational surfaces inside the plasma. The reported experimental results allow us to shed some light on the existence and importance of the 'staircase' phenomenon.

This article is organized as follows: Section 2 discusses the methods we have used. Section 3 presents the results for the rotational transform scan experiments. Section 4 interprets the results with the aid of a numerical turbulence model. In Section 5 we draw some conclusions.

2. Methods

The TJ-II stellarator is a flexible Heliac [12] with toroidal magnetic field $B_T \simeq 1$ T, major radius $R_0 = 1.5$ m and minor radius $a < 0.22$ m [10]. In the experiments discussed here, plasmas were heated using two ECRH beam lines delivering up to 300 kW each at a frequency of 53.2 GHz (X mode).

In the following, we briefly describe the tools we used in this study. Section 2.1 presents the principles of the rotational transform scan; although experimental details are given in Section 3. Section 2.2 describes the probe systems and discusses the analysis techniques used. Section 2.3 provides a summary of the calculation and interpretation of the intermittence parameter, $C(1)$. Section 2.4 describes a Resistive MHD turbulence model we use to help interpret the results.

2.1. Rotational transform scan

To perform the experiments described below, we make use of a rather unique feature of the TJ-II stellarator: namely, its capacity to perform dynamical scans of the magnetic configuration. This capacity allows varying the characteristics of the magnetic configuration in vacuum, such as the rotational transform, plasma volume, magnetic well, etc. by varying the external coil currents. This variation is performed in a controlled manner during a single discharge [13]. In the experiments performed here, the offset of the rotational transform was varied linearly in time. This amounts to scanning the location of the rational surfaces radially, while keeping all other quantities almost constant. By performing measurements at a fixed radial position, quantities corresponding to some important plasma properties, such as pressure gradients, are also nearly constant at the measurement location. This way, the impact of the rotational transform on plasma properties can be studied almost without suffering from other confounding factors. In addition, these experiments offer an excellent resolution in terms of rotational transform that would be difficult to achieve by performing radially spaced measurements.

2.2. Probe systems

TJ-II is fitted with several probe systems. In the present study, we perform measurements with the so-called D probe, located at a toroidal angle of $\phi = 38.2°$. The reciprocating probe drive was fitted with the two-dimensional probe head shown in Fig. 1. It has a boron nitride body shaped as a double staircase, with sets of probes on various levels. Here, we will use one set of three pins on one staircase step (measuring $V_f, I_{\rm sat}, V_f$, repectively; V_f being the floating potential and $I_{\rm sat}$ the ion saturation current), aligned poloidally at a given radial position.

To perform the analyses presented below, knowledge of the precise location of the probe tips with respect to the magnetic configuration is essential. The physical position of the probe has been calibrated with respect to the vacuum vessel of TJ-II, with a

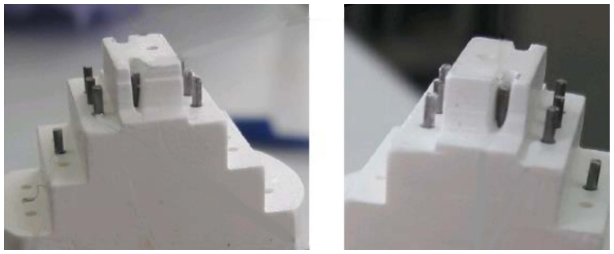

Figure 1. Langmuir probe head used in the present experiments.

precision of 1–2 mm. The magnetic configuration is mainly generated by currents flowing in the external coils, and various error sources may lead to geometric variations of up to about 6 mm with respect to theoretical expectations [14]. In addition, once the plasma is produced, small currents may flow inside the plasma that may affect the magnetic configuration [15]. Currents inside the plasma were kept small ($-0.6 < I_p < 0.1$ kA). A negative net plasma current may lead to a reduction of the rotational transform, $\iota = \iota/2\pi$, or in other words, move the rational surfaces out by a small distance. Considering the impact of all these error sources, the uncertainty of the probe position with respect to the expected location of the magnetic surfaces is at most ~ 1 cm.

An important quantifier in the framework of this paper is the poloidal rotation velocity, v_θ, at the probe location. Several alternative techniques for determining this quantity are available. One well-known procedure is to determine the velocity from the spectral 2-point $S(k,\omega)$ technique, given two poloidally spaced probe pins measuring the floating potential, V_f [16]. When applying this technique, based on Fourier transforms, we found that its statistical error (as measured by the scatter of obtained velocity values) was too large for our purposes, particularly in view of the fact that we need this quantity with a reasonable time resolution – of a few ms – in order to follow changes along the ι-scan that lasts 100 ms. A second technique is to measure the radial electric field, E_r, from two radially separated pins measuring V_f, and assuming that the rotation is dominated by the $E \times B$ drift, the poloidal velocity would follow from $v_\theta \simeq E_r/B$. Given the layout of the probe used, a suitable measurement of E_r was however not available. A final technique is to simply compute the cross correlation between two poloidally spaced V_f pins, $C(\Delta t)$. The poloidal velocity then follows immediately from $v_{\rm corr} \simeq d/\Delta t_{\rm max}$, where d is the poloidal probe separation and $\Delta t_{\rm max}$ is the time lag of the maximum value of C. This simple technique suffers from low resolution: although the sampling frequency of the V_f measurements is high, $f_{\rm samp} = 2$ MHz, the probe distance is only $d = 6$ mm, so the directly accesible values of the velocity through this technique based on discretely sampled data are given by the set $v_{\rm corr} = d \cdot f_{\rm samp}/n$, such that $n \in \mathbb{Z}_{\neq 0}$, which is rather crude for velocities with expected values of several km/s. This limitation can be partly alleviated by improving the estimate of the location of the maximum of the correlation curve $C(\Delta t)$ using interpolation, noting that the maximum correlation value is generally quite high for these discharges, so that this can be done reliably: $\max(C) > 0.85$. For this purpose, we selected part of the $C(\Delta t)$ curve around

its discrete maximum, performed a cubic spline interpolation and then recalculated the time lag of the maximum from the interpolated spline curve. A drawback of this technique is that the presence of rotating, large MHD islands can affect the detected time delay: any such mode, if it has a sufficiently large amplitude, would cause the time delay to be determined by the phase structure of the (rotating) island, even at radial locations relatively far from the island location, rather than the local propagation of turbulent structures. Fortunately, in these discharges, no such large amplitude coherent modes were present; this was checked by inspecting the power spectra of the Langmuir probe signals and external Mirnov pick-up coils.

The radial electric field at the edge of the plasma was modified by applying a constant voltage to a biasing electrode, inserted to a position of $\rho \simeq 0.85$ [17].

2.3. Intermittence

In this work, we make use of a quantifier of intermittence originating in chaos theory [18, 19]. The method for calculating this quantity from time series is described elsewhere [11]. The 'intermittence parameter', $C(1)$, which takes on values between 0 and 1, is a measure of the 'burstiness' of a signal. We note that 'bursty' signals often (though not always) have a probability distribution with a kurtosis exceeding 3 (the kurtosis of a Gaussian distribution).

The meaning of the intermittence parameter $C(1)$ has been clarified in a recent study [20]. For our purposes, it is sufficient to know that $C(1)$ tends to be low when a single (helical) mode dominates the turbulence, leading to monofractal behaviour, and high when several modes interact, leading to multifractality. Such a 'dominant helical mode' is understood to be a locally dominant helical instability, which may be unsaturated and incoherent, not necessarily a saturated MHD island. Assuming data correspond to a fixed measurement location, the presence of a significant flow of the turbulent field past the observation point may also lead to an increase of multifractality and $C(1)$, as this will lead to a mixing between the temporal and spatial structure of the mode. In other words, $C(1)$ is both sensitive to mode dominance and flow velocity. Mode dominance is determined to some degree by the presence of low-order rational surfaces, provided the drive (gradient) is such that the corresponding helical modes are triggered. In view of the above, in some circumstances and with some caveats $C(1)$ can be used to determine the location of important low-order rationals, as shown in recent work [21].

2.4. Modelling

To understand the behaviour reported in the following, we performed turbulence simulations using a Resistive MHD turbulence model we have used before to interpret experimental results from the TJ-II [22, 23] and W7-X [24] stellarators.

The dominant instability in relatively low temperature stellarators is the resistive interchange mode. This mode is driven by the pressure gradient and in the nonlinear

regime it generates flow vortices and magnetic islands associated with singular surfaces. Since growth rates are higher for low m/n modes, low m/n modes are typically dominant. Such a dominant mode will produce flat spots in the pressure profile – typically broader for lower order – and lead to a 'staircase' profile, as described in [4]. This flattening (reduction of gradient) stabilizes the ideal MHD modes at the singular surface. In [3] it was shown that such 'staircase' profiles allow stability at higher overall plasma pressure, explaining why the experimental beta limit tends to be higher than the beta limit calculated using smooth profiles.

Dominant low-order modes are associated with flow patterns, producing vortices associated with the singular surfaces. These vortices generate zonal flows through Reynolds stress [25], thus producing local transport barriers. If the perturbation stream function, i.e., the fluctuation of the potential, is radially symmetric with respect to the position of the singular surface, the zonal flow (proportional to the derivative of the potential) is asymmetric, i.e., zero at the surface but with a maximum on one side a minimum on the other. Contrarily, if the potential fluctuation is antisymmetric, the zonal flow has a maximum at the singular surface. As we will see, the cases studied here, the potential fluctuation is symmetric.

The numerical model is based on the reduced MHD equations [26], in which pressure gradient modes provide the main instability drive. The model is evolved in periodic cylinder geometry, with minor radius a and length $L = 2\pi R_0$. The corresponding coordinate system is (r, θ, ζ), where r is the cylindrical radius, θ the poloidal angle, and $\zeta = z/R_0$, where z is the axial cylinder coordinate. Thus, when the cylinder is bent in a torus, ζ corresponds to an effective toroidal angle. The model equations describe the evolution of (a) the poloidal magnetic flux ψ, (b) the z component of the vorticity of the flow, U, by means of a momentum balance equation, (c) the density n and (d) the electron temperature T_e. Including the evolution of the magnetic flux is essential to understand the interaction of the turbulence with helical modes. The evolving quantities are decomposed in Fourier series in the poloidal and toroidal angles, whereas the radial component is evaluated using finite differences. Given the limitations of this numerical model, the numerical calculations do not constitute a full and detailed simulation of these TJ-II plasmas, although they do reproduce many of their salient features. For more details, please refer to Ref. [27].

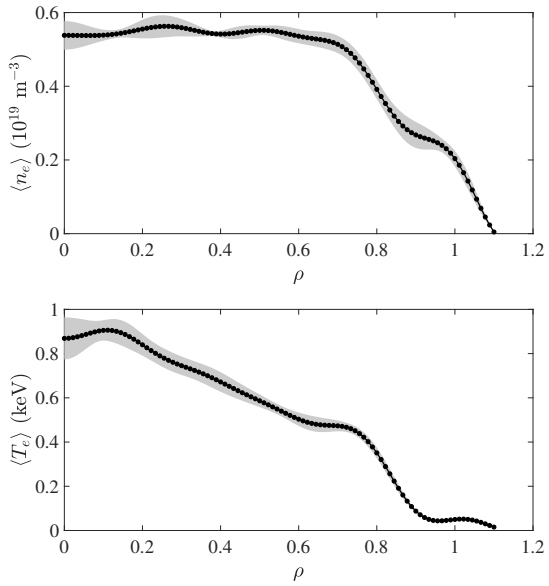

Figure 2. Mean profiles of electron density (top) and electron temperature (bottom), reconstructed using a Bayesian method [28] using Thomson Scattering, Helium beam and interferometry data.

3. Rotational transform scan experiments

The dynamic rotational transform scans were performed by varying the external coil currents linearly over a time interval of 100 ms during the plasma steady state phase ($1100 \leq t \leq 1200$ ms). ECR heating power was approximately 2×250 kW. Currents flowing inside the plasma were kept small using a current control system. The line average density of these plasmas was low ($\overline{n}_e \simeq 0.5 \cdot 10^{19}$ m^{-3}). Electron density profiles were rather flat in the core region ($\rho \lesssim 0.6$) and fell off gradually to the plasma edge for $\rho \gtrsim 0.7$. Electron temperature profiles were peaked with $T_e(0) \simeq 1$ keV. Mean profiles, calculated from Thomson Scattering, interferometry, and Helium Beam data using a Bayesian method [28], are shown in Fig. 2. Low radial wavenumber oscillations in these profiles are an artifact of the method used and should not be taken into account. Profiles remain roughly constant while the rotational transform is varied gradually over a rather narrow range, as reflected in the constancy of several important plasma quantifiers (see below).

In these conditions, the plasma is in the so-called Neoclassical electron root state, such that the radial electric field E_r is predominantly positive [29]. In view of these conditions and the resulting low plasma pressure ($\beta < 0.1\%$), flux surfaces are almost unaffected by Shafranov shift effects [28]. Consequently, external control of the magnetic configuration is very good and flux surface and rotational transform modifications due to plasma pressure and plasma current are small [30]. Fig. 3 shows two ι profiles (in vacuum), corresponding to the start (lower) and end (upper) profile of the ι-scan. The shape of these ι profiles is very similar, except for an offset. Please note the vertical

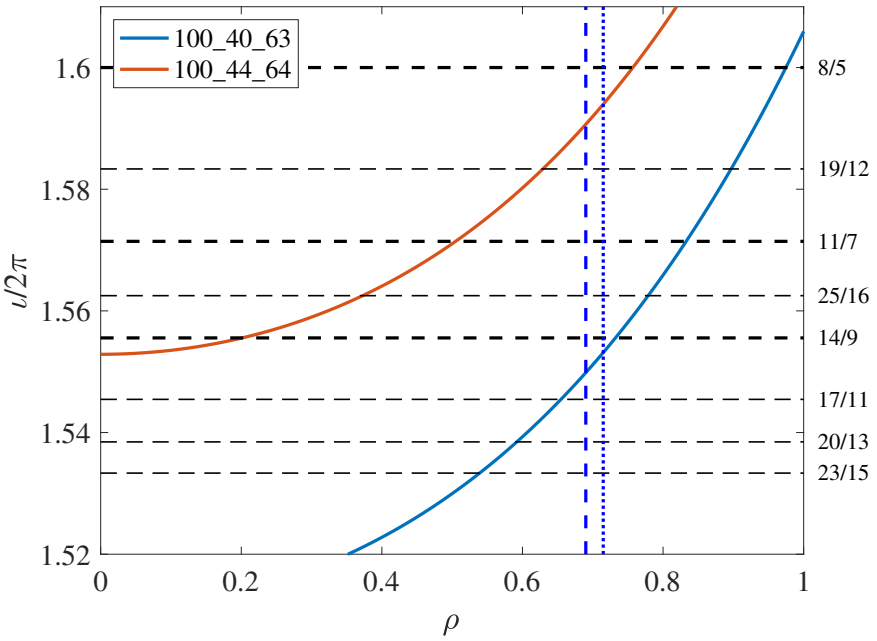

Figure 3. The rotational transform, $\iota/2\pi$, for the two vacuum magnetic configurations corresponding to the scan end points. Some relevant rational values of $\iota/2\pi$ are indicated by means of horizontal dashed lines. The probe location is indicated by vertical blue lines (dotted line: nominal position; dashed line: corrected position – see text).

scale of the figure: in spite of the apparent large gap between the lower and upper ι profiles, the difference is in fact rather small, so that global confinement conditions are almost unchanged.

3.1. The impact of biasing

Fig. 4 shows the dependence of the plasma line average density, $\overline{n}_e$, and net plasma current, I_p, on the applied biasing voltage, $V_{\rm pol}$. The error bars correspond to the variation within a discharge rather than a measurement error. The line average density was very constant, both within each discharge and between discharges. The small plasma current I_p also did not vary significantly ($\simeq -0.22$ kA on average).

The voltage applied to the biasing probe was varied between discharges. Fig. 5 shows the temporal average of the poloidal velocity $\langle v_{\rm corr}\rangle$ versus the applied biasing potential, $V_{\rm pol}$. The poloidal velocity $\langle v_{\rm corr}\rangle$ at the Langmuir probe position was calculated using the spline interpolated correlation technique discussed in Section 2.2. The temporal average was taken over the time window of interest, $1100 \leq t \leq 1200$ ms. There is a definite and systematic relation between the applied biasing and the resulting poloidal velocity. The shape of this curve is due to the exponential $I-V$ characteristic of Langmuir probes [31]: at positive $V_{\rm pol}$, the biasing probe is able to drive significant (radial) current, leading to a corresponding modification of the poloidal rotation velocity,

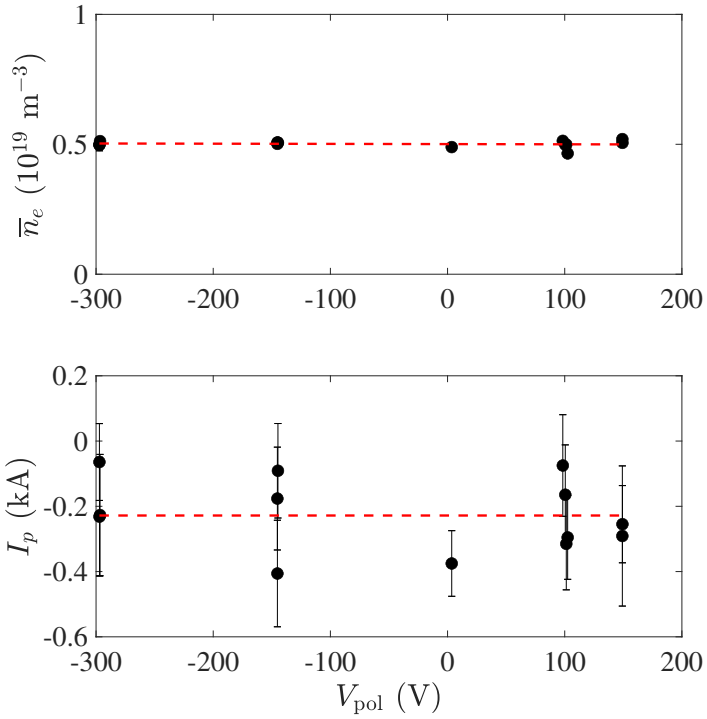

Figure 4. Dependence of the plasma line average density, $\overline{n}_e$, and net plasma current, I_p, on the applied biasing voltage, $V_{\rm pol}$.

whereas at negative $V_{\rm pol}$, the driven current and the corresponding modification of the poloidal rotation velocity is small. An exponential fit, $\langle v_{\rm corr}\rangle = A + B\exp(V_{\rm pol}/T_e)$, yields $T_e \simeq 70$ eV, which is a reasonable value for the edge electron temperature.

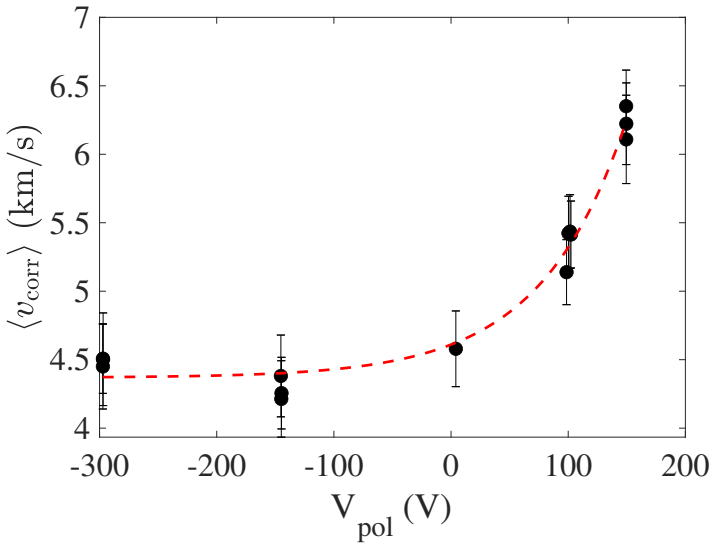

Figure 5. Effect of applied biasing (horizontal axis) on the temporal mean value of the poloidal velocity at the probe location (vertical axis). Each dot corresponds to a discharge. Error bars are an estimate of random variations with respect to the smoothed temporal evolution. The dashed line is an exponential fit.

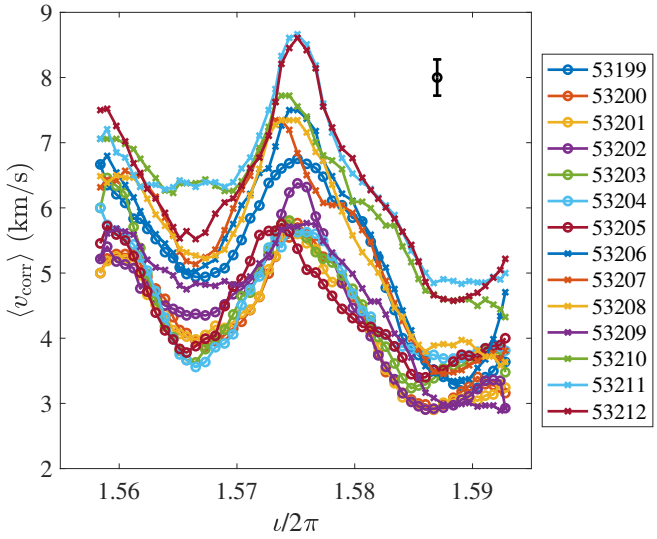

Figure 6. Poloidal velocity at the probe location. The horizontal axis corresponds to the calculated rotational transform value at the nominal location of the probe as the rotational transform profile is scanned. The typical error bar of these data is indicated inside the figure, top right.

3.2. Poloidal velocity, intermittence and probe position correction

Fig. 6 shows the measured poloidal velocity at the Langmuir probe, using the spline interpolated correlation technique discussed in Section 2.2, for the set of discharges considered. The horizontal axis shows the ι value at the nominal, fixed location of the probe as the ι-profile is scanned (see Fig. 3). One observes that the poloidal velocity is modulated strongly along the ι-scan, by about 30% or more. There is also a vertical shift of the curves from one shot to the next, which is associated with the applied biasing (see Fig. 5).

As noted in Section 2.2, the relative probe position with respect to the magnetic configuration is subject to some uncertainty. Consequently, Fig. 6 should not be used to infer any association between the poloidal velocity pattern and rotational transform values or rational surfaces. This issue can be clarified using the intermittence of the floating potential signal, which is known to drop when low-order modes, associated with low-order rational surfaces, are dominant [20]. Fig. 7 shows an interpolated representation of the intermittence, $C(1)$, on the same axes as Fig. 6. Black dots represent the location of actual data points, the color patches represent the linear interpolation between the points of the intermittence. An interesting pattern appears, similar in some important respects to the modelling results shown below in Fig. 15. The main feature is a general minimum of $C(1)$ that occurs around $\iota_{\rm nominal} \simeq 1.575$ for most of the discharges studied. From the modelling result, we expect this minimum to correspond approximately to the location of an important rational surface, the only candidate being the 11/7 surface ($\iota \simeq 1.571$), located close by.

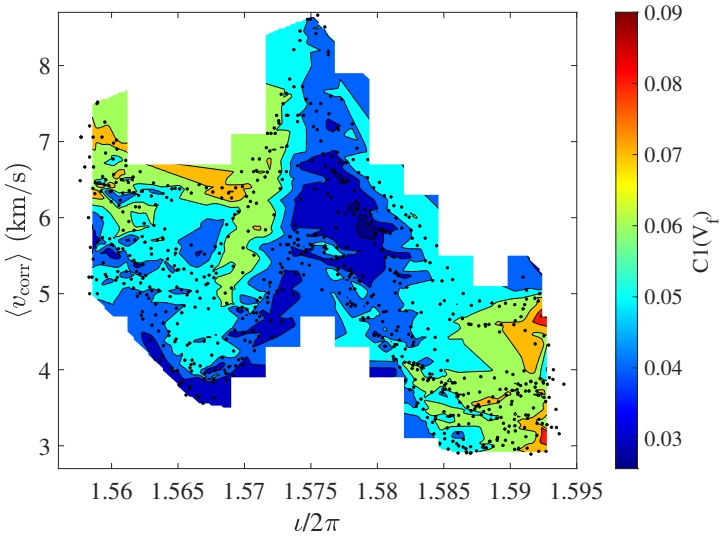

Figure 7. Intermittence, $C(1)$ at the probe location. Black dots correspond to the data points shown in Fig. 6, colors represent the interpolation of $C(1)$ values determined at those points.

Given the positioning error of the probe as discussed in Section 2.2, and taking into account that the small negative plasma current (Fig. 4) would reduce ι [15] such that the passage of a given rational surface across the probe position would be slightly delayed, we are justified to apply an additional shift of ι to ensure that the $C(1)$ minimum coincides roughly with the 11/7 surface. The nominal and corrected positions are indicated by vertical dashed lines in Fig. 3. Applying this small shift, we obtain Fig. 8. We have drawn in the location of a few low order rational surfaces for clarity. The main minimum of the intermittence, $C(1)$, now corresponds approximately to the 11/7 rational, while a secondary minimum, although perhaps not well resolved, may occur at the 14/9 rational; noting that these are the two lowest-order rationals of the four shown.

Fig. 9 shows the poloidal velocity data of Fig. 6 after applying the position correction of the probe. The pattern of the poloidal velocity has 4 extrema in the ι-range studied, and each extremum corresponds to a low order rational surface. A similar effect is observed in a numerical model, as will be discussed in Section 4 below. Note that the rational surfaces are not equidistant, and the spacing between rationals corresponds nicely with the spacing of the extrema, giving additional confidence that this approach is valid.

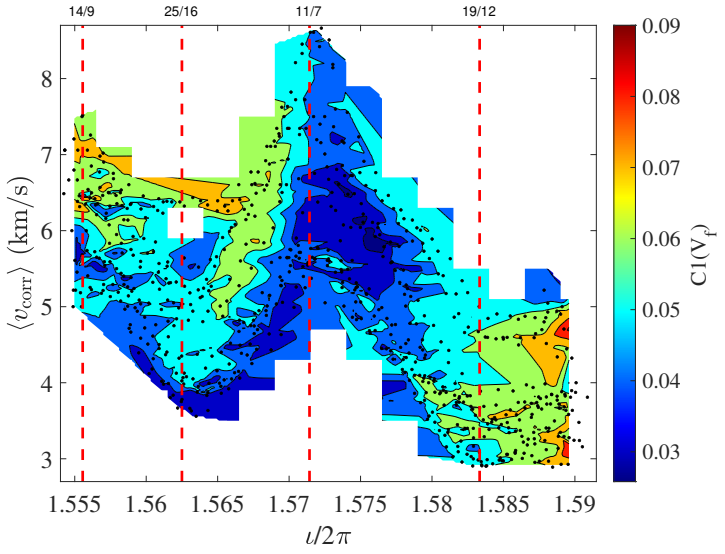

Figure 8. Intermittence at the corrected probe location. Some relevant rational values of ι are indicated by means of vertical dashed lines.

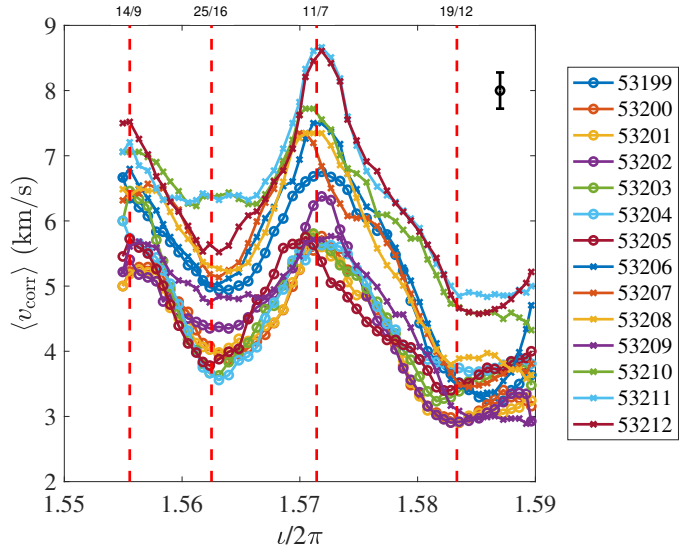

Figure 9. Poloidal velocity at the corrected probe location. Some relevant rational values of ι are indicated by means of vertical dashed lines. The typical error bar of these data is indicated inside the figure, top right.

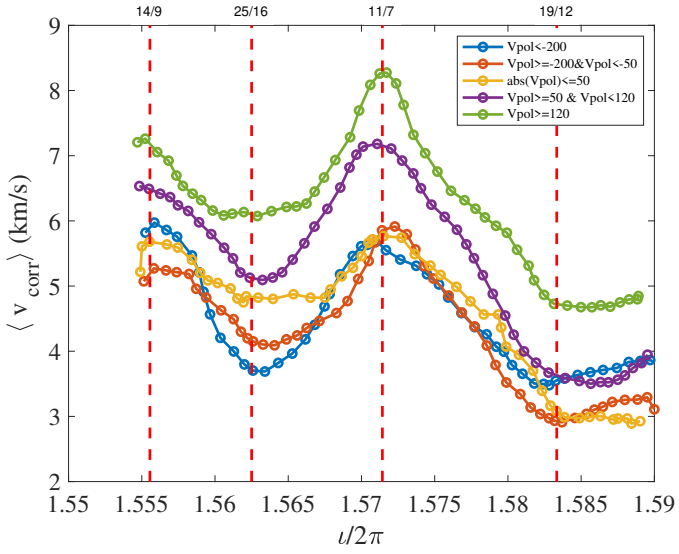

Figure 10. Dependence of the poloidal rotation profiles on ι and the applied biasing voltage, $V_{\rm pol}$ (V).

3.3. Impact of biasing and rationals on various quantifiers

To facilitate further analysis, in this section we group shots with a similar biasing voltage together and average over these grouped shots. We distinguish 5 groups. Fig. 10 shows the poloidal velocity, averaged over the grouped shots (see legend). This plot is an easier to read version of Fig. 9. The profile-averaged poloidal rotation behaves as seen in Fig. 5.

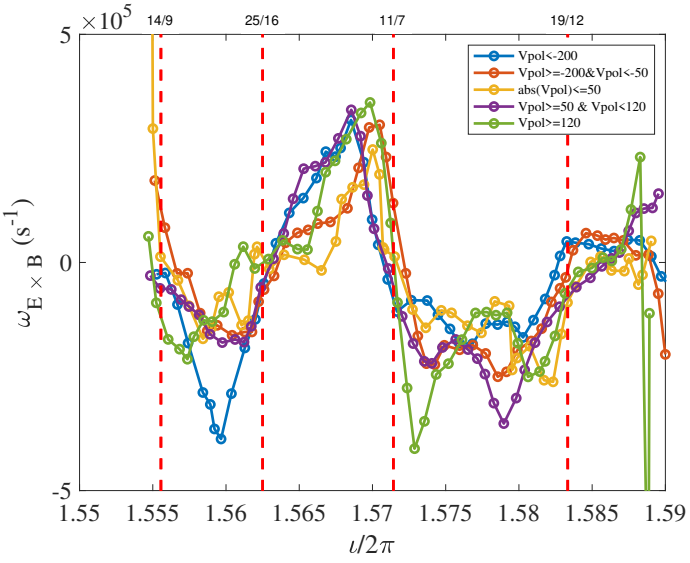

Figure 11. Dependence of the velocity shearing rate, $\omega_{E\times B}$, on ι and the applied biasing voltage, $V_{\rm pol}$.

Fig. 11 shows the estimated shearing rate, $\omega_{E\times B} = \frac{dv_\theta}{dr} \simeq \frac{1}{a}\frac{d\iota}{d\rho}\frac{dv_\theta}{d\iota}$. It does not appear to depend on the biasing. It has a clear radial dependence and zero crossings that match the locations of the rational surfaces. The competition between the turbulence growth rate, γ, and $\omega_{E\times B}$ is often assumed to be responsible for turbulence suppression in transport barriers [32]. Here, the turbulence growth rate is not known, but in some regions the absolute value of this parameter is sufficiently large ($\gtrsim 10^5$ s^{-1}) to potentially suppress turbulence [33].

Fig. 12 shows the mean value of the fluctuating particle flux, $\Gamma = C\langle \tilde{I}_{\rm sat}\tilde{E}_\theta\rangle$. The proportionality constant C has been set to 1, so the flux is given in arbitrary units. It has a 'radial' pattern (meaning a strong dependence on ι), which suggests the existence of minor transport barriers. The radial structure has a wavelength that suggests a relation with the spacing of the main low-order rationals as indicated, but there is no clear direct relation with $\omega_{E\times B}$ (Fig. 11), which may be due to the unknown pattern of the turbulence growth rate that also plays a part.

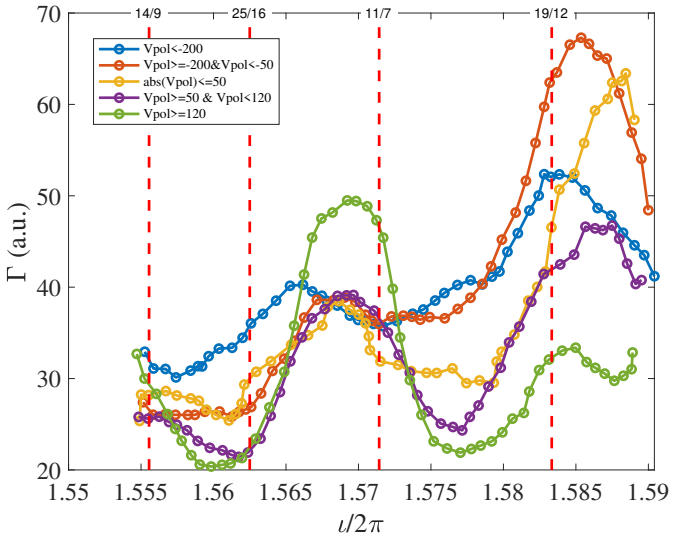

Figure 12. Dependence of the fluctuating particle flux on ι and the applied biasing voltage, $V_{\rm pol}$.

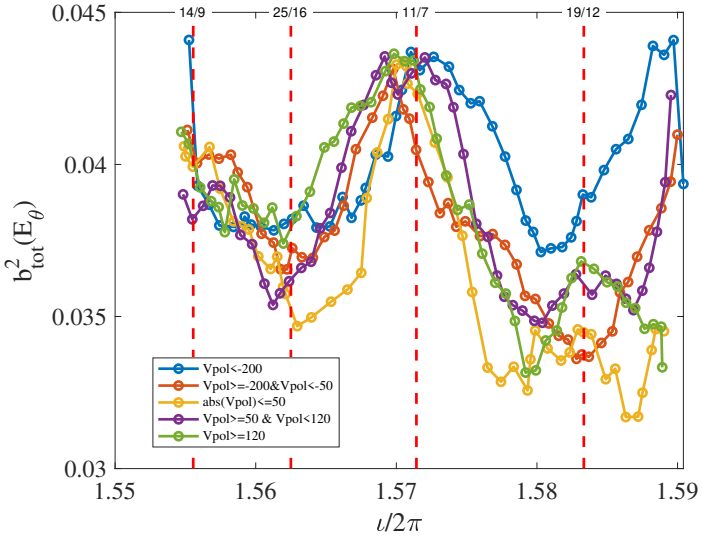

Figure 13. Dependence of the total bicoherence $b^2(E_\theta)$ on ι and the applied biasing voltage, $V_{\rm pol}$.

3.4. Bicoherence

To better understand the interaction between the MHD turbulence, associated with rational surfaces, and broad-band turbulence, we computed the bicoherence of the poloidal electric field E_θ, calculated from the difference of two poloidally displaced probe pins measuring V_f [34]. Fig. 13 shows the result, calculated using time windows of 2 ms, such that each time window is subdivided into 50 sub-windows to evaluate the Fourier spectra needed to evaluate the bicoherence. The total auto-bicoherence (i.e., integrated over the two-dimensional frequency space of the bicoherence) shows a small but systematic variation with ι. This indicates that MHD modes are mostly activated at the rational surfaces 14/7 and 11/7, and less so at 25/16 and 19/12, which could explain the pattern seen in Fig. 10. Note also that the bicoherence shows an increasing trend towards high ι values, which may be related to the presence of the important $\iota = 8/5$ surface, immediately outside the experimental range.

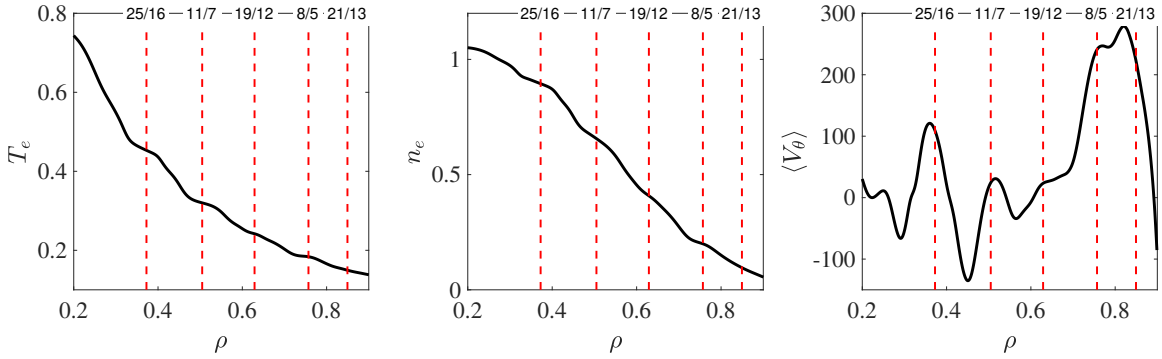

Figure 14. Profiles in the numerical model: temperature, density, and poloidal flow velocity.

4. Modelling results

To understand the results reported in Section 3, we turn to the Resistive MHD turbulence model described briefly in Section 2.4. Turbulence was calculated under conditions matching the 'standard' TJ-II configuration (labelled 100_44). Fig. 14 shows an example of steady state profiles obtained using this model. We note the appearance of small 'staircase' steps in the temperature and density profiles, associated with low order rational surfaces, and a corresponding strong modulation of the poloidal flow velocity. This happens because the pressure profile self-organizes to a state in which 'flat spots' appear around the most unstable (low order) rational surfaces, thus stabilizing the most unstable modes (see Section 2.4). It should be noted that the 'flat spots' are usually associated with steep gradient regions both inside and outside the flat spot, which could be considered 'transport barriers'.

Once a turbulent steady state was achieved, we applied a constant electric field, E_{r0}, in the region $0.5 < r/a < 1.0$, inducing additional poloidal rotation. We then continued to evolve the model to understand the impact of this electric field on the turbulence. This procedure was repeated for several values of E_{r0}, which effectively allows assessing the impact of the flux surface averaged poloidal flow velocity, $\langle v_\theta \rangle$, on the intermittence.

Fig. 15 shows maps of the resulting intermittence calculated from the fluctuating plasma potential, in the plane of poloidal velocity versus rotational transform. It is observed that the intermittence parameter $C(1)$ is minimal at the location of important low-order rational surfaces when $\langle v_\theta \rangle \simeq 0$. These results confirm the statements made in Section 2.3.

Comparing this result with the experimental results, Fig. 9, we observe a similar area of low $C(1)$ near the 11/7 rational surface. This area of low $C(1)$ occurs at $\langle v_{\rm corr} \rangle \simeq 6000$ m/s, not at 0 m/s; but note that there are no data for lower values of $\langle v_{\rm corr} \rangle$, so that it is not possible to clarify this point with the given data. In any case, the lowest values of $C(1)$ occur for the lowest values of $\langle v_{\rm corr} \rangle$ within the experimental range.

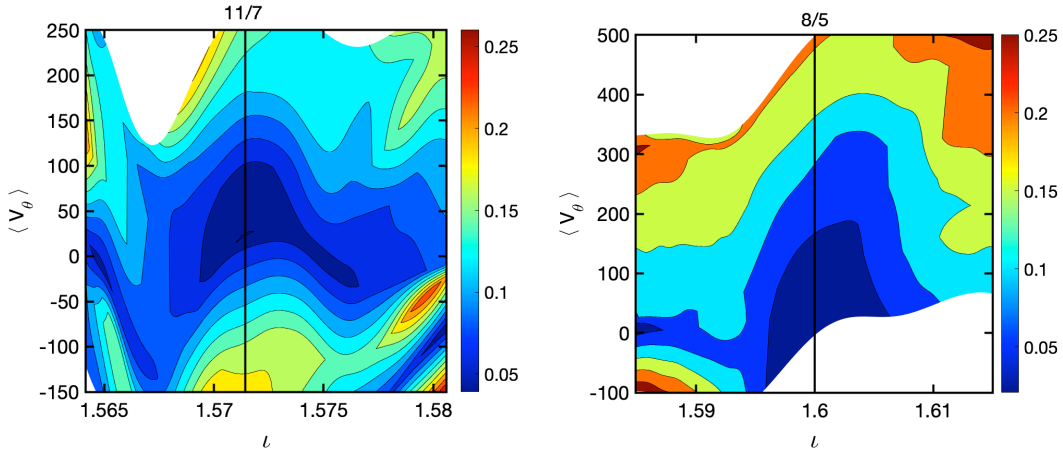

Figure 15. Modelling results: the intermittence parameter, $C(1)$, as a function of ι and the poloidal flow velocity, $\langle v_\theta \rangle$.

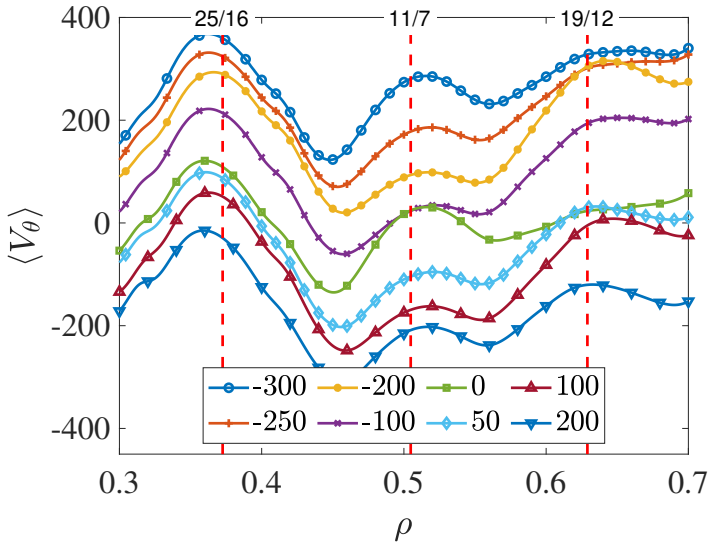

Figure 16. Mean (flux surface averaged) poloidal velocity, $\langle V_\theta \rangle$, versus normalized minor radius, for various values of the externally imposed radial electric field, E_r^0 (legend).

Fig. 16 shows the mean (flux surface averaged) poloidal velocity, $\langle V_\theta \rangle$, versus normalized minor radius, for various values of the externally imposed radial electric field, E_r^0. The overall pattern is similar to what is observed experimentally and reported in Fig. 10. In particular, there is an overall vertical velocity shift, proportional to the imposed E_r^0. Velocity maxima occur at the location of several important rational surfaces.

There is also an important difference: in this radial range, velocity peaks occur at all three indicated rationals, 25/16, 11/7, and 19/12. However, in the experimental result shown in Fig. 10, of these three only 11/7 corresponds to a maximum, whereas 25/16 and 19/12 correspond to a minimum. This difference is probably related to whether the

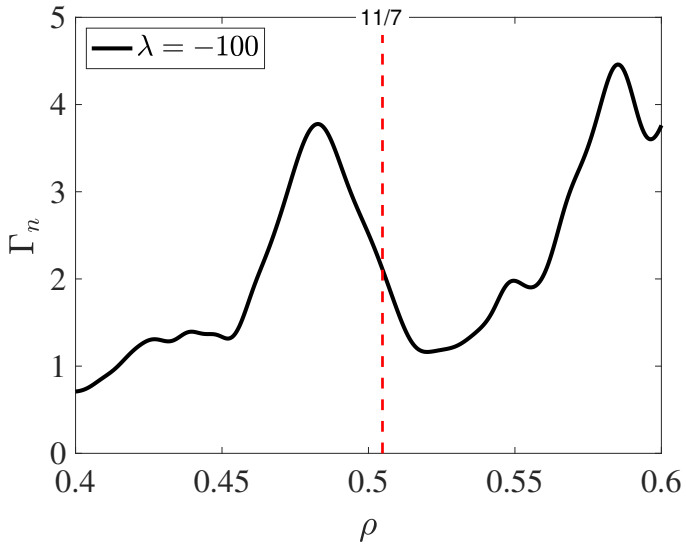

Figure 17. Particle flux near the 11/7 rational surface in the numerical model.

instability corresponding to the rational surface is triggered or not, which will depend on the local values of the thermodynamic driving gradients. In the simulation, the gradients will have been above the threshold value for each of these three rational surfaces, whereas in the experimental situation, the gradient was such as to trigger the instability of only the lowest order rational surfaces (11/7 and 14/9). This interpretation is corroborated by the bicoherence result shown in Fig. 13, which confirms that nonlinear mode coupling occurs mainly at the 11/7 and 14/9 rational surfaces.

The calculation can also help to understand the behaviour of the particle flux. Fig. 17 shows the radial dependence of the particle flux near the 11/7 rational surface. One observes that the flux peaks near, but not at, the rational surface. This behaviour is very similar to what is observed experimentally, as reported in Fig. 12.

5. Conclusions

This paper presents the results of a unique set of experiments in which the rotational transform profile was scanned dynamically in time, while external biasing was applied and the Langmuir probe was inserted deep into the plasma ($\rho \simeq 0.7$). This carefully designed experiment allowed exploring the properties of the turbulent plasma in the neighbourhood of various important low-order rational surfaces at constant values of the thermodynamic driving gradients, given that the probe position was fixed and plasma parameters were kept constant during the scan.

Intermittence: One of the turbulent parameters that was determined is the intermittence $C(1)$ of the fluctuating floating potential V_f. It was found to exhibit a minimum close to an important low-order rational (11/7). It is known that $C(1)$ tends to drop near important low-order rational surfaces when the corresponding helical mode is dominant. This allowed us to apply a correction to the probe position, which was known with an accuracy of about 1 cm, while the rational surfaces might in addition experience a slight outward shift due to the small net plasma current.

Flow pattern: A systematic and reproducible pattern was observed in the poloidal plasma flow velocity, $v_{\rm corr}$, determined from the correlation between poloidally displaced floating potential pins. After correction of the probe position relative to the rational surface 11/7, the pattern could be related to the rotational transform profile. The location of the extrema of the poloidal velocity was found to match the locations of the 4 lowest rational surfaces in the concerned rotational transform range perfectly (Fig. 10). When applying external constant biasing, the pattern of the flow $v_{\rm corr}$ remained unchanged except for an offset. The biasing also allowed studying the impact of the poloidal flow velocity on the measured intermittence.

The pattern could be understood on the basis of turbulence calculations performed with a Resistive MHD model. The poloidal flow $\langle V_\theta \rangle$ showed a similar offset and a similar pattern related to the location of low order rational surfaces (Fig. 16). In the simulations, the poloidal flow $\langle V_\theta \rangle$ peaked at each of the rationals 25/16, 11/7, and 19/12, whereas the experimental pattern only peaked at 14/9 and 11/7 and not at 25/16 and 19/12. We suggest that the pattern arises as a consequence of the relation between the driving gradient and the local turbulence threshold. In the model, the instabilities corresponding to all cited rationals are triggered, so that a velocity peak occurs at all rationals. Conversely, in the experiment, only the 14/9 and 11/7 instabilities are triggered. This hypothesis is corroborated by calculating the bicoherence (Fig. 13). The bicoherence detects the nonlinear coupling between low frequency modes and broad-band turbulence, and in this case peaks only at the 14/9 and 11/7 rational surfaces, whereas mode coupling is weaker or absent at the other rational surfaces (25/16 and 19/12).

Flux pattern: In addition, we observe a radial variation of the experimental fluctuating particle flux Γ. Regions of low Γ can be considered minor transport barriers for the fluctuating flux. The minima of Γ did, however, not coincide exactly with the

location of the low order rationals, neither in the experiment nor in the model. In any case, the radial structure has a radial wavelength that suggests a relation with the spacing of the main low-order rationals as indicated. The absence of a clear direct relation with $\omega_{E\times B}$ (Fig. 11) may be due to the fact that $\omega_{E\times B}$ is only part of the story; turbulence suppression is expected to occur when the turbulence growth rate γ is less than the shear suppression term $|\omega_{E\times B}|$ [32], and γ is not known here.

Staircase: Finally, it is appropriate to make a remark regarding the implications of the remarkable flow pattern observed here. In previous work, based on simulations, it was suggested that the pressure profile self-organizes to a state in which 'flat spots' appear around the most unstable (low order) rational surfaces [3, 4]. This self-regulation mechanism would allow achieving much higher global mean pressure values (β) than one might expect on the basis of smooth profiles. Fig. 14 illustrates this effect as seen in the calculations made in the context of the present paper. It is interesting to note that the corresponding pattern of flow variations is much more intense than the variations of pressure (or density or temperature) profiles. Due to experimental noise and limited radial resolution, one may expect that this effect is very hard to detect experimentally on the basis of the direct observation of pressure (or density or temperature) profiles [5]. On the other hand, measurement of the plasma (or floating) potential, the poloidal flow velocity, or the radial electric field may facilitate studying this effect.

This 'staircase', sometimes called the $E \times B$ staircase, has been observed in gyrokinetic simulations [8, 9]. The existence of this radial structure of E_r is expected to have a significant impact on transport, as it modulates the turbulent or 'anomalous' component of transport, interrupting the radial propagation of large transport events.

Acknowledgements

Research sponsored in part by the *Ministerio de Ciencia e Innovación* of Spain under project Nos. PID2019-110734RB-I00 and PID2021-124883NB-I00. This work has been carried out within the framework of the EUROfusion Consortium, funded by the European Union via the Euratom Research and Training Programme (Grant Agreement No 101052200 – EUROfusion). Views and opinions expressed are however those of the author(s) only and do not necessarily reflect those of the European Union or the European Commission. Neither the European Union nor the European Commission can be held responsible for them. B.A.C. gratefully acknowledges support for the research from the DOE office of Fusion Energy under U.S. Department of Energy Contract No. DE-SC0018076.

Data availabillity

The data that support the findings of this study are available from the corresponding author upon reasonable request.

ORCID codes

- B.P. van Milligen: ORCID 0000-0001-5344-6274
- I. Voldiner: ORCID 0000-0001-6703-7754
- B.A. Carreras: ORCID 0000-0001-7921-4690
- L. García: ORCID 0000-0002-0492-7466
- M.A. Ochando: ORCID 0000-0001-7521-4503

References

[1] I. Prigogine. *Order out of chaos: Man's new dialogue with Nature*. Bantam, New York, 1984.

[2] P.H. Diamond, S.-I. Itoh, K. Itoh, and T.S. Hahm. Zonal flows in plasma - a review. *Plasma Phys. Control. Fusion*, 47(5):R35, 2005. doi:10.1088/0741-3335/47/5/R01.

[3] B.A. Carreras, V.E. Lynch, K. Ichiguchi, T. Tatsumo, and M. Wakatani. On the β-limit induced by ideal interchange modes in stellarator configurations. *Plasma Phys. Reports*, 25(12):958, 1999.

[4] K. Ichiguchi and B.A. Carreras. Multi-scale MHD analysis incorporating pressure transport equation for beta-increasing LHD plasma. *Nucl. Fusion*, 51:053021, 2011. doi:10.1088/0029-5515/51/5/053021.

[5] N.J. Lopes Cardozo, G.M.D. Hogeweij, M. de Baar, C.J. Barth, M.N.A. Beurskens, F. De Luca, A.J.H. Donné, P. Galli, J.F.M. van Gelder, G. Gorini, B. de Groot, A. Jacchia, F.A. Karelse, J. de Kloe, O.G. Kruijt, J. Lok, P. Mantica, H.J. van der Meiden, A.A.M. Oomens, Th. Oyevaar, F.J. Pijper, R.W. Polman, F. Salzedas, F.C. Schüller, and E. Westerhof. Electron thermal transport in RTP: filaments, barriers and bifurcations. *Plasma Phys. Control. Fusion*, 39:B303, 1997. doi:10.1088/0741-3335/39/12B/023.

[6] A.M.R. Schilham, G.M.D. Hogeweij, and N.J. Lopes Cardozo. Electron thermal transport barriers in RTP: experiment and modelling. *Plasma Phys. Control. Fusion*, 43:1699, 2001. doi:10.1088/0741-3335/43/12/305.

[7] B.Ph. van Milligen, B. Carreras, L. García, and J. Nicolau. The radial propagation of heat in strongly driven non-equilibrium fusion plasmas. *Entropy*, 21(2):148, 2019. doi:10.3390/e21020148.

[8] G. Dif-Pradalier, G. Hornung, Ph. Ghendrih, Y. Sarazin, F. Clairet, L. Vermare, P.H. Diamond, J. Abiteboul, T. Cartier-Michaud, C. Ehrlacher, D. Estève, X. Garbet, V. Grandgirard, Ö.D. Gürcan, P. Hennequin, Y. Kosuga, G. Latu, P. Maget, P. Morel, C. Norscini, R. Sabot, and A. Storelli. Finding the elusive $E \times B$ staircase in magnetized plasmas. *Phys. Rev. Lett.*, 114:085004, 2015. doi:10.1103/PhysRevLett.114.085004.

[9] F. Rath, A. G. Peeters, and A. Weikl. Analysis of zonal flow pattern formation and the modification of staircase states by electron dynamics in gyrokinetic near marginal turbulence. *Physics of Plasmas*, 28(7):072305, 2021. doi:10.1063/5.0054358.

[10] C. Hidalgo, E. Ascasíbar, D. Alegre, A. Alonso, J. Alonso, R. Antón, A. Baciero, J. Baldzuhn, J.M. Barcala, L. Barrera, E. Blanco, J. Botija, L. Bueno, S. Cabrera, A. de Castro, E. de la Cal, I. Calvo, A. Cappa, D. Carralero, R. Carrasco, B. Carreras, R. Castro, A. de Castro, L. Cebrián, A.A. Chmyga, M. Chamorro, P. Colino, F. de Aragón, M. Drabinskiy, J. Duque, L. Eliseev, F.J. Escoto, T. Estrada, M. Ezzat, F. Fraguas, D. Fernández-Ruiz, J.M. Fontdecaba, A. Gabriel, D. Gadariya, L. García, I. García-Cortés, R. García-Gómez, J.M. García-Regaña, A. González-Jerez, G. Grenfell, J. Guasp, V. Guisse, J. Hernández-Sánchez, J. Hernanz, A. Jiménez-Denche, P. Khabanov, N. Kharchev, R. Kleiber, F. Koechl, T. Kobayashi, G. Kocsis, M. Koepke, A.S. Kozachek, L. Krupnik, F. Lapayese, M. Liniers, B. Liu, D. López-Bruna, B. López-Miranda, U. Losada, E. de la Luna, S.E. Lysenko, F. Martín-Díaz, G. Martín-Gómez, E. Maragkoudakis, J. Martínez-Fernández, K.J. McCarthy, F. Medina, M. Medrano, A.V. Melnikov, P. Méndez, F.J. Miguel, B. van Milligen, A. Molinero, G. Motojima, S. Mulas, Y. Narushima, M. Navarro, I. Nedzelskiy, R. Nuñez, M. Ochando, S. Ohshima, E. Oyarzábal, J.L. de Pablos, F. Palomares, N. Panadero, F. Papoušek, F. Parra, C. Pastor, I. Pastor, A. de la Peña, R. Peralta, A. Pereira, P. Pons-Villalonga, H. Polaino, A.B. Portas, E. Poveda, F.J. Ramos, G.A. Rattá, M. Redondo, C. Reynoso, E. Rincón, C. Rodríguez-Fernández, L. Rodríguez-Rodrigo, A. Ros, E. Sánchez, J. Sánchez, E. Sánchez-Sarabia, S. Satake, J.A. Sebastián, R. Sharma, N. Smith, C. Silva, E.R. Solano, A. Soleto, M. Spolaore, T. Szepesi, F.L. Tabarés, D. Tafalla, H. Takahashi, N. Tamura, H. Thienpondt, A. Tolkachev, R. Unamuno, J. Varela, J. Vega, J.L. Velasco, I. Voldiner, S. Yamamoto, and the TJ-II Team. Overview of the TJ-II stellarator research

programme towards model validation in fusion plasmas. *Nuclear Fusion*, 62(4):042025, 2022. doi:10.1088/1741-4326/ac2ca1.

[11] B.A. Carreras, V.E. Lynch, D.E. Newman, R. Balbín, J. Bleuel, M.A. Pedrosa, M. Endler, B. van Milligen, E. Sánchez, and C. Hidalgo. Intermittency of plasma edge fluctuation data: Multifractal analysis. *Phys. Plasmas*, 7(8):3278, 2000. doi:10.1063/1.874193.

[12] J.H. Harris, J.L. Cantrell, T.C. Hender, B.A. Carreras, and R.N. Morris. A flexible heliac configuration. *Nucl. Fusion*, 25(5):623, 1985. doi:10.1088/0029-5515/25/5/005.

[13] D. López-Bruna, J.A. Romero, R. Jiménez-Gómez, M.A. Pedrosa, M. Ochando, T. Estrada, A. López-Fraguas, F. Medina, J. Herranz, T. Kalhoff, E. Ascasíbar, A. de la Peña, F. Lapayese, and J. Alonso. First dynamic magnetic configuration scans in ECRH plasmas of the TJ-II heliac. *Nucl. Fusion*, 49:085016, 2009. doi:10.1088/0029-5515/49/8/085016.

[14] E. Ascasíbar, J. Qin, and A. López-Fraguas. Magnetic surface mapping experiments in TJ-II heliac. *J. Plasma Fusion Res. SERIES*, 1:183, 1998.

[15] D. López-Bruna, F. Castejón, T. Estrada, J.A. Romero, J.A. Jiménez, E. Ascasíbar, and the TJ-II Team. Effects of ohmic current in the TJ-II stellarator. *Nucl. Fusion*, 44:645, 2004. doi:10.1088/0029-5515/44/5/008.

[16] D. E. Smith and E. J. Powers. Experimental determination of the spectral index of a turbulent plasma from digitally computed power spectra. *The Physics of Fluids*, 16(8):1373–1374, 1973. doi:10.1063/1.1694524.

[17] C. Silva, B. Goncalves, M. A. Pedrosa, C. Hidalgo, K. McCarthy, E. Calderon, J. Herranz, I. Pastor, and O. Orozco. Transport and fluctuations during electrode biasing on TJ-II. *Czech. J. Phys.*, 55(12):1589, 2005. doi:10.1007/s10582-006-0044-3.

[18] C. Meneveau and K.R. Sreenivasan. Simple multifractal cascade model for fully developed turbulence. *Phys. Rev. Lett.*, 59:1424, 1987. doi:10.1103/PhysRevLett.59.1424.

[19] C. Meneveau and K.R. Sreenivasan. The multifractal nature of turbulent energy dissipation. *J. Fluid Mechanics*, 224:429, 1991. doi:10.1017/S0022112091001830.

[20] B.A. Carreras, L. García, J.H. Nicolau, B.Ph. van Milligen, U. Hoefel, M. Hirsch, and the TJ-II and W7-X Teams. Intermittence and turbulence in fusion devices. *Plasma Phys. Control. Fusion*, 62:025011, 2020. doi:10.1088/1361-6587/ab57f9.

[21] B. Ph. van Milligen, B.A. Carreras, L. García, and C. Hidalgo. The localization of low order rational surfaces based on the intermittence parameter in the TJ-II stellarator. *Nucl. Fusion*, 60:056010, 2020. doi:10.1088/1741-4326/ab79cc.

[22] L. García, B.A. Carreras, V.E. Lynch, M.A. Pedrosa, and C. Hidalgo. Sheared flow amplification by vacuum magnetic islands in stellarator plasmas. *Phys. Plasmas*, 8(9):4111, 2001. doi:10.1063/1.1392996.

[23] B.Ph. van Milligen, J.H. Nicolau, L. García, B.A. Carreras, C. Hidalgo, and the TJ-II Team. The impact of rational surfaces on radial heat transport in TJ-II. *Nucl. Fusion*, 57(5):056028, 2017. doi:10.1088/1741-4326/aa611f.

[24] B.Ph. van Milligen, U. Hoefel, J.H. Nicolau, M. Hirsch, L. García, B.A. Carreras, C. Hidalgo, and the W7-X Team. Study of radial heat transport in W7-X using the transfer entropy. *Nucl. Fusion*, 58(7):076002, 2018. doi:10.1088/1741-4326/aabf5d.

[25] B.A. Carreras, V.E. Lynch, L. García, and P.H. Diamond. Resistive pressure-gradient-driven turbulence with self-consistent flow profile evolution. *Phys. Fluids B*, 5:1491, 1993. doi:10.1063/1.860889.

[26] H.R. Strauss. Nonlinear, three-dimensional magnetohydrodynamics of noncircular tokamaks. *Phys. Fluids*, 19:134, 1976. doi:10.1063/1.861310.

[27] B.Ph. van Milligen, B.A. Carreras, L. García, G. Grenfell, I. Voldiner, C. Hidalgo, and the TJ-II Team. The impact of radial electric fields and plasma rotation on intermittence in TJ-II. *Plasma Phys. Control. Fusion*, 64:055006, 2022. doi:10.1088/1361-6587/ac54e9.

[28] B.Ph. van Milligen, T. Estrada, E. Ascasíbar, D. Tafalla, D. López-Bruna, A. López-Fraguas, J.A. Jiménez, I. García-Cortés, A. Dinklage, R. Fischer, and the TJ-II Team. Integrated data analysis

at TJ-II: the density profile. *Rev. Sci. Instrum.*, 82(7):073503, 2011. doi:10.1063/1.3608551.

[29] J.L. Velasco, J.A. Alonso, I. Calvo, and J. Arévalo. Vanishing neoclassical viscosity and physics of the shear layer in stellarators. *Phys. Rev. Lett.*, 109(13):135003, 2012. doi:10.1103/PhysRevLett.109.135003.

[30] B.Ph. van Milligen, A. Lopez Fraguas, M.A. Pedrosa, C. Hidalgo, A. Martín de Aguilera, and E. Ascasíbar. Parallel and perpendicular turbulence correlation length in the TJ-II stellarator. *Nucl. Fusion*, 53:093025, 2013. doi:10.1088/0029-5515/53/9/093025.

[31] I.H. Hutchinson. *Principles of Plasma Diagnostics*. Cambridge University Press, New York, 2002.

[32] K.H. Burrell. Tests of causality: Experimental evidence that sheared $E \times B$ flow alters turbulence and transport in tokamaks. *Phys. Plasmas*, 6(12):4418, 1999. doi:10.1063/1.873728.

[33] C. Hidalgo, M.A. Pedrosa, L. García, and A. Ware. Experimental evidence of coupling between sheared-flow development and an increase in the level of turbulence in the TJ-II stellarator. *Phys. Rev. E*, 70:067402, 2004. doi:10.1103/PhysRevE.70.067402.

[34] B.Ph. van Milligen, T. Kalhoff, M.A. Pedrosa, and C. Hidalgo. Bicoherence during confinement transitions in the TJ-II stellarator. *Nucl. Fusion*, 48:115003, 2008. doi:10.1088/0029-5515/48/11/115003.